

# 2D Perovskites with Giant Excitonic Optical Nonlinearities for High-Performance Sub-Bandgap Photodetection

Feng Zhou, Ibrahim Abdelwahab, Kai Leng, Kian Ping Loh,\* and Wei Ji\*

Two-dimensional (2D) perovskites have proved to be promising semiconductors for photovoltaics, photonics, and optoelectronics. Here, a strategy is presented toward the realization of highly efficient, sub-bandgap photodetection by employing excitonic effects in 2D Ruddlesden–Popper-type halide perovskites (RPPs). On near resonance with 2D excitons, layered RPPs exhibit degenerate two-photon absorption (D-2PA) coefficients as giant as 0.2–0.64 cm MW<sup>-1</sup>. 2D RPP-based sub-bandgap photodetectors show excellent detection performance in the near-infrared (NIR): a two-photon-generated current responsivity up to  $1.2 \times 10^4$  cm<sup>2</sup> W<sup>-2</sup> s<sup>-1</sup>, two orders of magnitude greater than InAsSbP-pin photodiodes; and a dark current as low as 2 pA at room temperature. More intriguingly, layered-RPP detectors are highly sensitive to the light polarization of incoming photons, showing a considerable anisotropy in their D-2PA coefficients ( $\beta_{[001]}/\beta_{[011]} = 2.4$ , 70% larger than the ratios reported for zinc-blende semiconductors). By controlling the thickness of the inorganic quantum well, it is found that layered RPPs of  $(C_4H_9NH_3)_2(CH_3NH_3)Pb_2I_7$  can be utilized for three-photon photodetection in the NIR region.

Searching for materials that efficiently interact with light through nonlinear optical (NLO) processes has been a subject of intense research for many years. Among various NLO processes,<sup>[1]</sup> two-photon absorption (2PA), as a third-order NLO process, has been widely utilized in sub-bandgap photodetection<sup>[2]</sup> by converting light with photon energies ( $h\nu$ ) below the bandgap ( $E_g$ ) of a semiconductor into electrical signals. Such nonlinear sub-bandgap photodetection is highly desirable for applications in optical communication, solar energy harvesting, and quantum technology.<sup>[3–6]</sup> Relying on the fact that the 2PA photon-to-current efficiency increases either with decreasing  $E_g$  or increasing transition dipole moment ( $\mu$ ),<sup>[7,8]</sup> most of the commercially available 2PA detectors are based on narrow-bandgap semiconductors that operate in the mid-infrared (mid-IR) spectral

Dr. F. Zhou, Prof. W. Ji  
 Department of Physics  
 National University of Singapore  
 Singapore 117551, Singapore  
 E-mail: phyjiwei@nus.edu.sg

Dr. F. Zhou, Dr. I. Abdelwahab, Dr. K. Leng, Prof. K. P. Loh  
 Department of Chemistry  
 National University of Singapore  
 Singapore 117546, Singapore  
 E-mail: chmlohkp@nus.edu.sg

Dr. I. Abdelwahab, Dr. K. Leng, Prof. K. P. Loh  
 Center for Advanced 2D Materials and Graphene Research Centre  
 Singapore 117546, Singapore

Dr. I. Abdelwahab, Prof. K. P. Loh  
 NUS Graduate School for Integrative Sciences and Engineering  
 National University of Singapore  
 Singapore 117546, Singapore

Dr. K. Leng, Prof. K. P. Loh  
 Solar Energy Research Institute of Singapore (SERIS)  
 Singapore 117574, Singapore

Prof. K. P. Loh, Prof. W. Ji  
 SZU-NUS Collaborative Innovation Centre for Optoelectronic  
 Science and Technology  
 International Collaborative Laboratory of 2D Materials for Optoelectronic  
 Science and Technology of Ministry of Education  
 College of Optoelectronic Engineering  
 Shenzhen University  
 Shenzhen, Guangdong 518060, P. R. China

 The ORCID identification number(s) for the author(s) of this article  
 can be found under <https://doi.org/10.1002/adma.201904155>.

DOI: 10.1002/adma.201904155

region.<sup>[9,10]</sup> In addition, hyper-doped semiconductors with enhanced  $\mu$  have been also employed for sub-bandgap detection at a temperature of 10 K.<sup>[7]</sup> However, the third-order NLO response of the conventional nonlinear materials is inherently weak, hindering the development of efficient nonlinear photodetectors that can function in a room-temperature environment. Sub-bandgap detection through NLO at shorter-wavelengths (e.g., near-IR) has also remained challenging.

Recently, 2D hybrid organic–inorganic perovskites (HOIPs) have commanded major research interests due to their fascinating optical and electronic properties.<sup>[11–14]</sup> An archtypical class of these hybrid materials is the 2D Ruddlesden–Popper-type halide perovskite (RPP), which is constructed from alternately stacked molecular sheets of organic cation and inorganic perovskite anion with the general formula  $(RNH_3)_2A_{(n-1)}B_nX_{3n+1}$  (where  $R \geq 4C$ , A = monovalent organic cation, e.g.,  $CH_3NH_3^+$ ,  $NH_2CHNH_2^+$ , B = divalent metal cation, e.g.,  $Pb^{2+}$ ,  $Sn^{2+}$ , and X =  $I^-$ ,  $Br^-$ ,  $Cl^-$ ). The electronic landscape of 2D RPPs can be widely tuned by controlling the nature of the cationic and anionic species and/or by enlarging the thickness of the quantum well, i.e., increasing the number of inorganic layers (increasing  $n$  in the formula) within each quantum well. Practically, the bandgap of RPPs can be tuned over the entire near-UV/visible range by subtle variations in the RPP composition and stoichiometry.<sup>[11]</sup> Furthermore, the optical properties of 2D RPPs are essentially dominated by excitonic resonances due to the strong quantum and dielectric confinement effects introduced by the organic barrier layers.<sup>[15–17]</sup>

The strong light-matter interaction in 2D RPPs makes it possible to attain exceptionally high optical nonlinearity at subwavelength scales, opening new opportunities for ultrathin efficient nonlinear optical devices. Indeed, efficient nonlinear processes including self-phase modulation<sup>[18]</sup> and third-harmonic generation<sup>[19]</sup> with large third-order NLO susceptibilities enhanced by the large dipole moment associated with the excitonic transitions have been recently demonstrated for 2D perovskites. Along the same lines, the optical transition dipole moments involved in the RPP's 2PA excitonic-resonant process are expected to be large, and would result in desirable 2PA coefficients.<sup>[20,21]</sup> Based on a recently reported quantum theory on 2D excitons,<sup>[21,22]</sup> we can derive an approximation for the degenerate 2PA (D-2PA) coefficient ( $\beta$ ) associated with near-resonant 2p-excitonic states as

$$\beta_{G \rightarrow 2p} = K \frac{NM^2(\epsilon + 2)^4}{E_{2p}\Gamma_{2p}} a_B^4 \quad (1)$$

Here,  $N$  is the density of active unit cells,  $M^2$  interprets the probability of forming the 1s-exciton in a 2D material,  $\epsilon$  is the electric permittivity,  $E_{2p}$  and  $\Gamma_{2p}$  are the 2p-exciton energy and the line-width, respectively,  $a_B$  is the effective Bohr radius of the 2D exciton, and  $K$  is a material-independent constant which has a value of  $3 \times 10^{10}$  in the units such that  $\beta_{G \rightarrow np}$  is in  $\text{cm MW}^{-1}$ ,  $N$  is in  $\text{cm}^{-3}$ ,  $E_{2p}$  and  $\Gamma_{2p}$  are in eV, and  $a_B$  is in meters (Derivation details can be found in Supporting Information). As suggested by Equation (1), both large values of  $NM^2$  and large Bohr radius ( $a_B$ )<sup>[23,24]</sup> are preferable for efficient

excitonic-resonant 2PA processes, if one selects 2D RPPs. The D-2PA coefficients of 2D RPPs are calculated to be on the order of  $0.3\text{--}2.5 \text{ cm MW}^{-1}$  per monolayer in the spectral range from  $0.8$  to  $1.6 \mu\text{m}$ . Previous studies into the NLO properties of 2D RPPs have mainly been carried out on polycrystalline films and powders.<sup>[25]</sup> The presence of grain boundaries and trap states in these polycrystalline samples typically downgrades the RPP crystal quality and hides its intrinsic NLO properties.

On the other hand, single crystals of the butylammonium lead halide of RPP crystals as  $(\text{C}_4\text{H}_9\text{NH}_3)_2(\text{CH}_3\text{NH}_3)_n\text{Pb}_n\text{I}_{3n+1}$  ( $n=1,2,3,4$ ) have been demonstrated to possess a very low density of defects and/or traps within the bandgap<sup>[26]</sup> and a high internal quantum efficiency ( $\approx 34\%$ ) in the  $0.3\text{--}0.8 \mu\text{m}$  spectrum.<sup>[26\text{--}29]</sup> Promisingly, the recent advances in micromechanical cleavage of RPP single crystals have enabled the isolation of 2D RPP nanosheets with superior optical properties. Furthermore, inorganic quantum wells in RPP nanosheets would increase the effective length of light-matter nonlinear interaction, especially for the excitonic-resonant 2PA process. By taking advantage of these material properties, we have constructed two-photon detectors based on layered  $(\text{C}_4\text{H}_9\text{NH}_3)_2(\text{CH}_3\text{NH}_3)_3\text{Pb}_4\text{I}_{13}$  ( $n=4$ ), as illustrated in Figure 1, for the detection of femtosecond laser pulses in the spectrum of  $0.8\text{--}1.6 \mu\text{m}$ . We find that these detectors show excellent detection performance: a two-photon current (2 PC) responsivity up to  $1.2 \times 10^4 \text{ cm}^2 \text{ W}^{-2} \text{ s}^{-1}$ , two orders of magnitude greater than the standard InAsSbP-pin photodiode,<sup>[9]</sup> and a dark current as low as  $2 \text{ pA}$  at room temperature. More intriguingly, our 2D-RPP-based detectors are sensitive to light polarization of incoming photons, showing a considerably

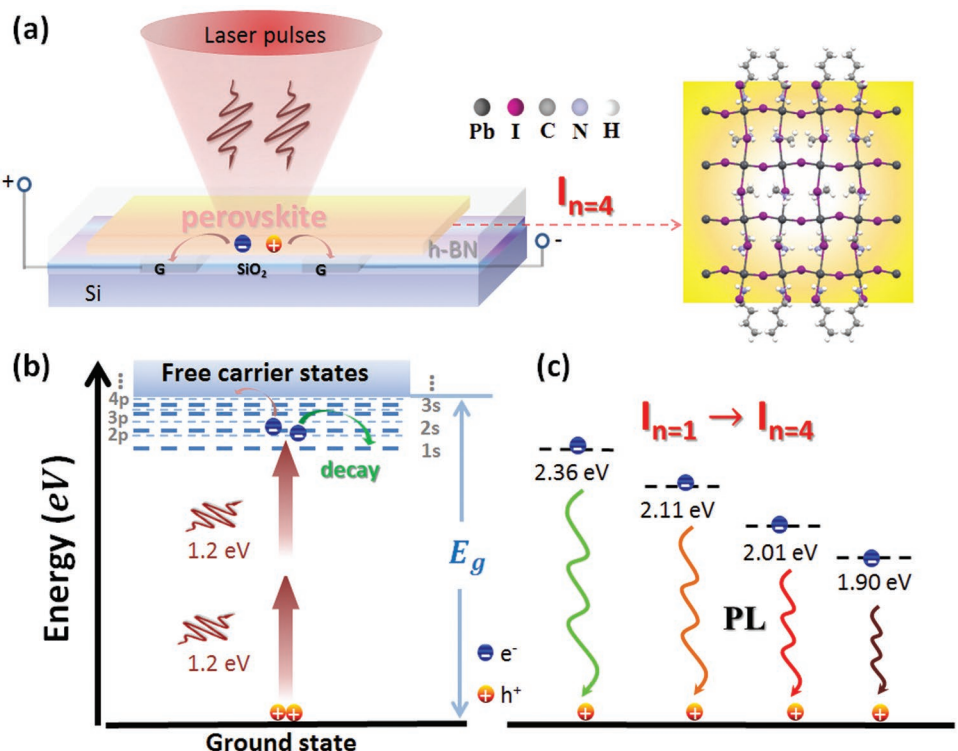


**Figure 1.** a) Schematic representation of sub-bandgap photodetection based on 2D Ruddlesden–Popper halide perovskites (2D-RPPs). Right: A side view of the molecular structure for monolayer 2D-RPPs ( $I_{n=4}$ ). b) Energy level diagram for degenerate two-photon absorption (D-2PA) and subsequently, either nonradiative decay to 1s state or disassociation to free carriers. c) Photoluminescence (PL) for 2D-RPPs ( $I_{n=1,2,3,4}$ ).

large anisotropy in its D-2PA coefficients ( $\beta_{[001]}/\beta_{[011]} = 2.4$ , 70% more than the ratios reported in literature).<sup>[30]</sup> We also demonstrate that layered perovskites of  $(C_4H_9NH_3)_2(CH_3NH_3)Pb_2I_7$  ( $I_{n=2}$ ) can be utilized for three-photon detection in the 1.3–1.6  $\mu m$  range.

To validate our strategy, we designed and fabricated bottom-contact RPP-based phototransistors, as schematized in Figure 1a. High-quality, homologous single crystals of  $(C_4H_9NH_3)_2PbI_4$  ( $I_{n=1}$ ),  $(C_4H_9NH_3)_2(CH_3NH_3)Pb_2I_7$  ( $I_{n=2}$ ),  $(C_4H_9NH_3)_2(CH_3NH_3)_2Pb_3I_{10}$  ( $I_{n=3}$ ), and  $(C_4H_9NH_3)_2(CH_3NH_3)_2Pb_4I_{13}$  ( $I_{n=4}$ ) were synthesized by a temperature-programmed crystallization method.<sup>[19,26]</sup> Furthermore, the phase purity of the as-grown large-sized RPP ( $I_{n=1,2,3,4}$ ) crystals was confirmed to be single phase by X-ray diffraction (XRD) as reported in the previous work.<sup>[26]</sup> Their optical characterizations are shown in Figure S1 in the Supporting Information. The centimeter-sized RPP single crystals were then exfoliated to yield thin flakes (nanosheets) and transferred onto prepatterned substrates. Fabrication specifics can be found in the Experimental Section. In our RPP-based phototransistors, graphene electrodes were applied to achieve low Schottky barriers as previously reported.<sup>[31,32]</sup> Under the illumination of laser pulses in the near-infrared region,  $np$ -excitons ( $n = 2, 3, \dots$ )

are created through the D-2PA process. Intrinsically, the  $np$ -excitons (or electron–hole pairs) can either decay to the lowest excitonic states (1s-exciton)<sup>[33]</sup> or dissociate to form free charge carriers at room temperature,<sup>[34]</sup> as shown in Figure 1b. The former leads to 2PA-excited photoluminescence (2PPL), see Figure 1c, while the latter generates sub-bandgap photocurrents under a bias voltage.

To demonstrate the large optical nonlinearities of 2D RPPs, we carried out 2PPL measurements with a confocal microscope, see details in the Experimental Section. Thin flakes of 2D-RPP crystals ( $I_{n=1,2,3,4}$ ) were prepared on quartz substrates and encapsulated with protective layers of hexagonal boron nitride (h-BN), see Figure S2a–d in the Supporting Information. The h-BN encapsulation provides excellent protection from environmental factors such as photooxidation<sup>[35]</sup> and humidity.<sup>[36]</sup> Using 1030 nm ( $\approx 1.2$  eV) femtosecond laser pulses with 1 MHz repetition rate as an excitation source, these thin flakes showed 2PPL with spectral peaks at 525, 587, 618, and 653 nm, respectively, see Figure 2. These 2PPL peaks correspond to the lowest excitonic energy levels for each RPP ( $I_{n=1,2,3,4}$ ) and are consistent with those excited by 1PA, as shown in Figure S1 in the Supporting Information. As an example, Figure 2b shows a square dependence of 2PPL

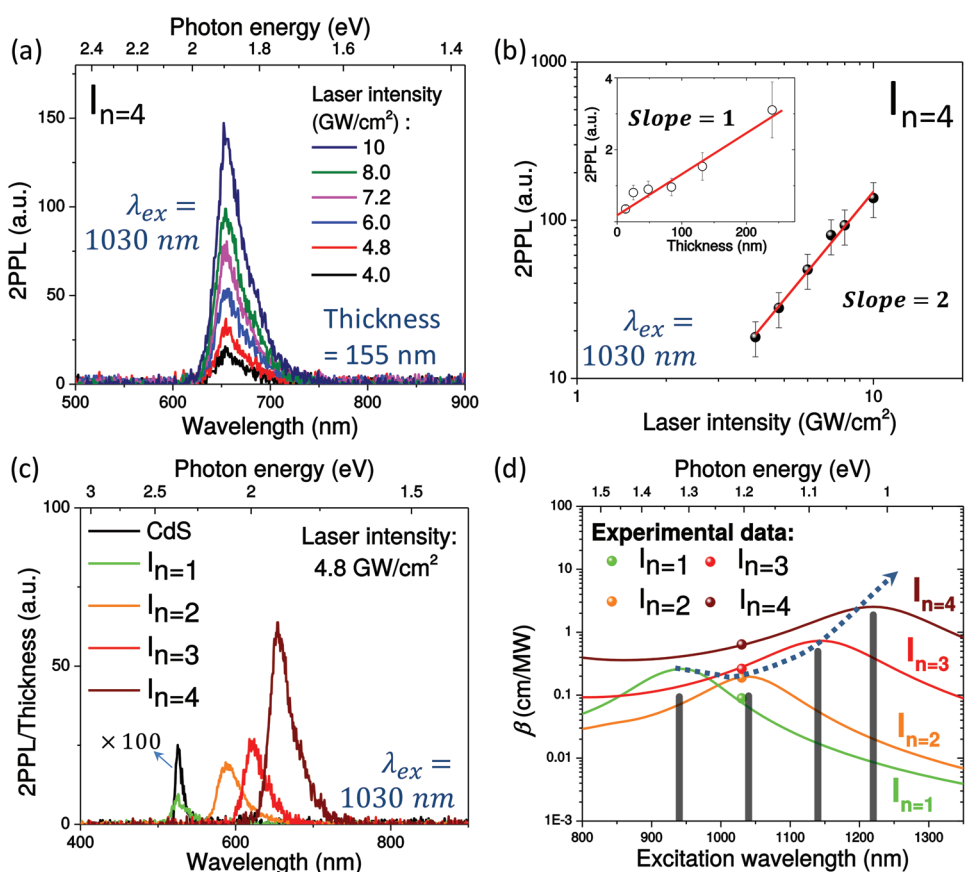


**Figure 2.** a) 2PPL spectra for a 155 nm thick flake of 2D-RPP ( $I_{n=4}$ ). b) 2PPL versus laser intensity on the log–log scale for the 155 nm thick flake. Inset: Thickness dependence of 2PPL for flakes of 2D-RPP ( $I_{n=4}$ ). c) 2PPL spectra measured on the 316 nm thick ( $I_{n=1}$ ), 582 nm thick ( $I_{n=2}$ ), 154 nm thick ( $I_{n=3}$ ), 155 nm thick ( $I_{n=4}$ ), and 0.5 mm thick bulk CdS. The 2PPL peaks are normalized by their thickness. d) Experimentally measured (colored dots) and theoretically calculated (colored curves) D-2PA spectra. The vertical bars indicate approximated D-2PA coefficients using Equation (1). The laser intensity is defined here as the maximum intensity of the laser pulses after considering the surface's Fresnel loss.

on the laser intensity, satisfying the energy-conservation law in D-2PA. The experimental results also demonstrated that the interaction length can be scaled up to at least 250 nm, see inset in Figure 2b. It was expected as the excited volume is proportional to the thickness ( $\approx L \cdot \pi \omega_0^2$ ). To obtain the D-2PA coefficient of our thin RPP crystals, the 2PPL signal from a bulky CdS crystal ( $5 \times 5 \times 0.5 \text{ mm}^3$ ) was used under the same setup as a reference.

The D-2PA coefficients of the 2D-RPP crystals can be determined by Equation (2)

$$\frac{\text{Signal of 2PPL (RPP)}}{\text{Signal of 2PPL (CdS)}} \propto \frac{(\eta\beta)_{\text{RPP}} \cdot L \cdot \pi \omega_0^2}{(\eta\beta)_{\text{CdS}} \cdot 2Z_o \cdot \pi \omega_0^2} \quad (2)$$

Here,  $Z_o = 12 \mu\text{m}$  is the Rayleigh length;  $\eta$  is the quantum efficiency of 2PPL, which is estimated to be 26%<sup>[11]</sup> and 10%<sup>[37]</sup> for 2D-RPP and CdS crystals, respectively; and  $\omega_0 = 2 \mu\text{m}$  is the spot radius of the focused laser beam. Because the CdS crystal thickness is much greater than the Rayleigh length, its effective volume of 2PPL is estimated to be  $\approx 2Z_o \cdot \pi \omega_0^2$ .

Figure 2d shows that the experimentally measured D-2PA coefficients are in good agreement with our theoretical-model (see the Supporting Information for more details). The excitonic-resonant D-2PA coefficients calculated by Equation (1) and shown as vertical bars in Figure 2d are also close to the experimental data, revealing that the dominant optical transitions are from 1s-excitons to 2p-excitons. For comparison, the D-2PA coefficients of our single-crystalline 2D-RPPs, especially the higher homologues  $(\text{C}_4\text{H}_9\text{NH}_3)_2(\text{CH}_3\text{NH}_3)_3\text{Pb}_4\text{I}_{13}$  ( $I_{n=4}$ ), are much higher than previously reported values for polycrystalline (powder) or bulk perovskites<sup>[25,38]</sup> and nondegenerate (ND) 2PA in traditional semiconductors, e.g., GaN, GaAs, and ZnSe,<sup>[3]</sup> refer to Table S2 in the Supporting Information for comparison with other nonlinear materials. As suggested by Equation (1), if the operating temperature is cooled down to 77 K where the linewidth ( $\Gamma_{2p}$ ) would decrease, and hence, the D-2PA coefficient would increase further by at least one order of magnitude.<sup>[22]</sup>

We selected 2D-RPPs ( $I_{n=4}$  and  $I_{n=2}$ ) for sub-bandgap photodetection measurements because their theoretically calculated D-2PA coefficients exhibit the maximal or minimal peak values, respectively. Figure 3a,b shows the optical images of our 2D-RPP ( $I_{n=4}$  and  $I_{n=2}$ ) devices. A femtosecond laser system with the pulse duration of  $\approx 150 \text{ fs}$  (full-width at half maximum, FWHM) and a repetition rate of 1 kHz was used, see the details in the Experimental Section. In optimizing the performance of phototransistor devices, 2D-RPP-based phototransistors were first positioned at the laser beam focal plane, and thereafter the laser beam was adjusted laterally (along either x- or y-axis in the focal plane), see the laser spot in Figure 3a, where a maximum signal in the photocurrent was observed. The photocurrent was measured directly with a low-noise source-meter (Keithley, 2636B)—no sophisticated means of detection (e.g., mode-locking or transimpedance amplifier) was required.

Upon the pulsed laser illumination, our bottom-contacted, 2D-RPP-based phototransistors became conductive due to photoexcited carriers, see the  $I_{\text{on}}/I_{\text{off}}$  ratio in Figure 3c. With a back-gate voltage ( $V_g$ ) of 0 V and a drain-source voltage ( $V_{ds}$ ) of 1 V, our 2D-RPP  $I_{n=4}$  devices exhibit an extremely high sensitivity at room temperature where the noise current is  $\approx 2 \text{ pA}$

and a corresponding noise equivalent energy of 0.4 nJ is inferred, see Figure 3c,d. The quadratic dynamic range (QDR) of effective pulse energy is measured to be from 0.4 to 3.5 nJ at a wavelength of 1200 nm, see Figure S4 in the Supporting Information.

As shown in Figure 3d, with an illumination wavelength of 600 nm ( $\approx 2.06 \text{ eV} > E_{1s} = 1.90 \text{ eV}$ ) on the 2D-RPP ( $I_{n=4}$ ) device, the one-photon-generated current (1 PC) predominates in the photocurrent generation, resulting in a fit-line slope of 1.0. The 1 PC responsivity of  $0.3 \text{ mA W}^{-1}$  can be derived from a division of the photocurrent by the average laser power (that is, the product of laser pulse energy and repetition rate). As the laser wavelength is tuned from 800 to 1600 nm ( $h\nu/E_{2p} = 0.4\text{--}0.8$ ), the fit-line slopes are  $\approx 2$ , an evidence for 2 PC processes. By analyzing the response in this region, we can extract the 2 PC responsivity as:  $\gamma_{2PC} = \frac{I_{PC}}{e} \frac{A}{P^2} (T \cdot \tau)^{[9]}$  where  $I_{PC}$  is the generated photocurrent,  $P$  is the average laser power, and  $A = 18 \times 5 \mu\text{m}^2$  is the active area of the photodetection,  $T$  is the repetition rate of the laser pulse,  $\tau$  is the pulse duration. As shown in Figure 3f, the measured 2 PC responsivity is in the range of  $(0.2 - 1.2) \times 10^4 \text{ cm}^2 \text{W}^{-2} \text{s}^{-1}$ . The maximum  $\gamma_{2PC}$  is achieved at 1200 nm ( $\approx 1.03 \text{ eV}$ ), that is nearly the half of  $E_{2p} = 2.003 \text{ eV}$ , consistent with the near-resonant of D-2PA coefficients calculated in Figure 2d. By normalizing the data of the flake thickness, each  $I_{n=4}$  single layer is found to possess a D-2PA coefficient as large as  $2.5 \text{ cm MW}^{-1}$ .

For comparison with a (3D perovskite)  $\text{CH}_3\text{NH}_3\text{PbBr}_3$ -based two-photon detector ( $\gamma_{2PC}$  estimated at  $\approx 4.6 \times 10^3 \text{ cm}^2 \text{W}^{-2} \text{s}^{-1}$  at 800 nm),<sup>[38]</sup> our maximum value of  $\gamma_{2PC}$  is one order of magnitude larger. Furthermore, the maximal  $\gamma_{2PC}$ -value is also significantly larger than those of a commercial InAsSbP-pin photodiode ( $\approx 580 \text{ cm}^2 \text{W}^{-2} \text{s}^{-1}$  at  $8 \mu\text{m}$ ), a commercial InAsSbP-photoresistor ( $\approx 69 \text{ cm}^2 \text{W}^{-2} \text{s}^{-1}$  at  $8 \mu\text{m}$ ),<sup>[10]</sup> and a GaN-based, ND-2PA detector ( $\gamma_{2PC} = 0.45 \text{ cm}^2 \text{W}^{-2} \text{s}^{-1}$  at 390 nm).<sup>[3]</sup> Interestingly, our 2D-RPP ( $I_{n=4}$ ) detector responds better than the previously reported monolayer MoS<sub>2</sub> detector<sup>[21]</sup> (see Table 1), despite that its D-2PA coefficient is less than that of monolayer MoS<sub>2</sub> as shown in Table S2 in the Supporting Information. This better performance can be attributed to the thickness independent direct bandgaps of 2D RPPs that lead to efficient excitonic-resonant D-2PA in 15 layers, while MoS<sub>2</sub> shows direct bandgap only at the monolayer level. However, limited by the near-infrared photon energy, the 2D RPP flake thickness, and the excitonic linewidth at room temperature, the performance of our 2D-RPP  $I_{n=4}$  detector in terms of the 2 PC responsivity is not superior to two-photon detector based on silicon hydrogenic donors.<sup>[7]</sup>

More interestingly, a distinct polarization dependence of 2 PC manifests itself in Figure 4 which plots the oscillation of 2 PC with periodicity of  $\theta = 90^\circ$  as the incident laser's polarization vector is rotated. In our experimental geometry,  $\theta$  is the angle between the polarization vector and the [001] crystallographic axis direction when laser pulses propagate in the perpendicular direction to the quantum well. We find that 2 PC reaches the maximum value when the polarization vector is parallel to the [001] direction. As the polarization direction changes from the [001] direction to the [011] direction, the 2 PC decreases systematically. Accordingly, the minimum value

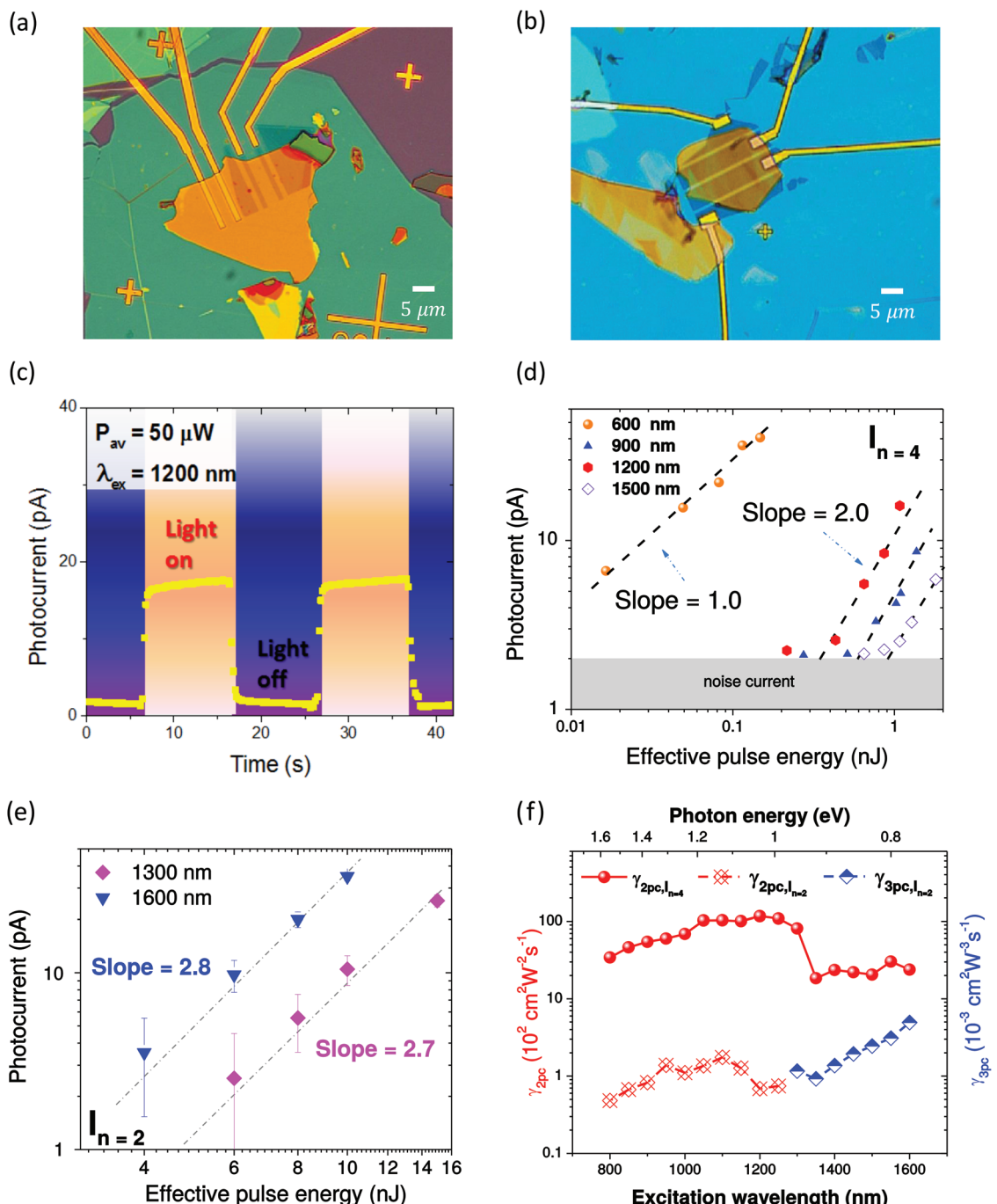


**Figure 3.** a,b) Optical images of the 2D-RPP ( $I_{n=4}$  and  $I_{n=2}$ ) device, respectively. Both  $I_{n=4}$  and  $I_{n=2}$  devices are encapsulated with few-layer h-BN (in green or in blue) for highly stable performance. The circular region in white illustrates the laser spot, where a maximum signal in the photocurrent was observed. c) Photoswitching behavior under alternating ON and OFF laser pulses for the 2D-RPP ( $I_{n=4}$ ) device. d,e) Photocurrent versus effective laser pulse energy on the log-log scale for the 2D-RPP ( $I_{n=4}$  and  $I_{n=2}$ ) device, respectively. f) 2 PC spectral responsivity (in red) of the 2D-RPP ( $I_{n=4}$  and  $I_{n=2}$ ) devices and 3 PC spectral responsivity (in blue) of the 2D-RPP ( $I_{n=2}$ ) device.

of 2 PC is obtained when polarization vector is parallel to the [011] direction. The ratio of the maximum to minimum 2 PC is  $I_{2PC,[001]}/I_{2PC,[011]} = 2.4$ .

As reported in ref. [26], the crystal of 2D-RPP ( $I_{n=4}$ ) adopts orthorhombic centered structure at room temperature. The polarization-resolved 2 PC can be modeled<sup>[39]</sup> by  $\gamma = A\{1 + 2$

$[\sigma_1 \sin^4(\theta + \varphi) - \sigma_2 \sin^2(\theta + \varphi)]\}$  with anisotropy parameters  $\sigma_1 = 1.18$  and  $\sigma_2 = 1.01$ , see the red curves in Figure 4. Here,  $A$  is a constant that directly proportional to the third-order nonlinear susceptibility  $\chi^{(3)}$  and  $\varphi$  is the angular offset. In the tetragonal space group, the intrinsic in-plane permutation symmetry results in three independent  $\chi^{(3)}$  tensor elements,  $\chi_{xxx}^{(3)}, \chi_{xyy}^{(3)}$ ,

**Table 1.** Performance of sub-bandgap photodetection at room temperature.

Semiconductor	Area (thickness)	Spectral range [nm]	R.R. (FWHM) <sup>a)</sup>	2 PC responsivity ( $\gamma_{2pc}$ ) [ $\text{cm}^2 \text{W}^{-2} \text{s}^{-1}$ ]	Dark current	QDR <sup>b)</sup> [nJ]	Reference
(C <sub>4</sub> H <sub>9</sub> NH <sub>3</sub> ) <sub>2</sub> (CH <sub>3</sub> NH <sub>3</sub> ) <sub>3</sub> Pb <sub>4</sub> I <sub>13</sub> , (I <sub>n=4</sub> )	18 × 5 $\mu\text{m}^2$ (80–90 nm)	800–1600	1 kHz (150 fs)	(0.2–1.2) × 10 <sup>4</sup>	2 pA	0.4–3.5	This work
CH <sub>3</sub> NH <sub>3</sub> PbBr <sub>3</sub>	4.9 × 3.3 mm <sup>2</sup> (3 mm)	800	76 MHz (100 fs)	4.6 × 10 <sup>3</sup>	N. A.	N. A.	[36]
MoS <sub>2</sub>	8 × 4 $\mu\text{m}^2$ (0.65 nm)	800–1100	1 kHz (150 fs)	(3–9) × 10 <sup>2</sup>	2 pA	10–80	[21]
GaN (ND-2PA)	0.25 mm <sup>2</sup> (5 $\mu\text{m}$ )	390 (signal) + 5600 (gate)	1 kHz (150 fs)	0.45	3.6 pA	N. A.	[3]
GaN (ND-2PA)	0.25 mm <sup>2</sup> (5 $\mu\text{m}$ )	5600 (signal) + 390 (gate)	1 kHz (150 fs)	0.048	3.6 pA	N. A.	[3]
InAsSbP	2 × 2 mm <sup>2</sup> (N.A.)	8000	10 Hz (10 ns)	69	1.5 nA	(1–20) × 10 <sup>3</sup>	[10]
InAsSbP-pin	$\pi × 0.15^2$ mm <sup>2</sup> (N.A.)	8000	10 Hz (10 ns)	580	4 nA	(1–20) × 10 <sup>3</sup>	[10]
Phosphorus atoms in Si	0.5 × 0.5 cm <sup>2</sup> (0.05 cm)	(6–7) × 10 <sup>4</sup> (or 4.25–4.88 THz)	25 MHz (100 ps)	3 × 10 <sup>9</sup> @10 K	N. A.	(0.05–2) × 10 <sup>3</sup>	[7]

<sup>a)</sup>R.R. (FWHM): Repetition rate (full-width at half maximum of laser pulses); <sup>b)</sup>QDR: Quadratic dynamic range.

and  $\chi_{xyy}^{(3)}$ ,<sup>[39,40]</sup> giving rise to the anisotropy in the 2 PC. Explicitly, Pb<sup>+</sup> and I<sup>-</sup> atoms in RPP crystals are connected by covalent bonds and form the tetragon lattice in plane. The orbitals of D-2PA generating *np*-excitons also follow the same orientation and thus result in the dichroism configurations for D-2PA as:  $\beta[001] = \frac{1}{1 - \sigma_1/2}$  and  $\beta[010] = \frac{1}{1 - \sigma_2/2}$ . Here,  $\beta[001] = \frac{3}{2} \frac{\omega}{\epsilon_0 n_0 c^2} \text{Im}[\chi_{xxxx}^{(3)}]$  is the D-2PA coefficient along the [001] direction, which is shown in Figure 2d. Compared to zinc-blende semiconductors, the effective D-2PA anisotropy of 2D-RPP (I<sub>n=4</sub>) is 70% greater.<sup>[30]</sup>

Interestingly, the 2D-RPP (I<sub>n=2</sub>) devices can perform either as a two-photon or a three-photon detectors depending on the laser wavelength. In the spectral range of 800–1250 nm, the photocurrent is predominated by D-2PA with fit-line slopes in the range of 1.8–2. The 2 PC responsivity is maximized at 1100 nm, with  $\gamma_{2pc} \approx 150 \text{ cm}^2 \text{ W}^{-2} \text{ s}^{-1}$ . This value is one order of magnitude less than I<sub>n=4</sub> counterparts which can be understood from the difference in their D-2PA coefficients, as shown in Figure 2d. On the other hand, the three-photon-absorption-generated photocurrents (3 PC) become predominant, as the laser wavelength is increased from 1300 to 1600 nm. The fit-slopes in the range of 2.7–2.9, see two examples in Figure 3e,

confirm that 3 PC predominates. The values of 3 PC responsivity are calculated by  $\gamma_{3pc} = \frac{I_{pc}}{e} \frac{A}{P^3} (T \cdot \tau)$  and shown by the blue symbols in Figure 3f. It is anticipated because of  $E_{1s}/3 < h\nu < E_{1s}/2$  and  $E_{1s}$  2.11 eV for 2D-RPP (I<sub>n=2</sub>). The results suggest that 3PC-based I<sub>n=2</sub> devices are efficient photodetectors in the spectral window of fiber-optical communications, indicating their potential use in telecommunications.

In summary, we have demonstrated that single-crystalline 2D RPP nanosheets exhibit extremely large D-2PA coefficients in the near-IR. The nonlinear response is enhanced near the two-photon resonances of the excitonic states, and the results are well consistent with the quantum perturbation theory on 2D excitons. We realize efficient polarization-resolved sub-bandgap photodetection at room temperature by utilizing 2D-RPP two-photon detectors. The 2D-RPP (I<sub>n=4</sub>) two-photon detector is found to have a very low noise equivalent energy, a giant 2 PC responsivity, and a significantly large anisotropic response. The 2D-RPP (I<sub>n=2</sub>) detector also performs as a predominated three-photon detector in the spectral range of 1300–1600 nm. The highly anisotropic sub-bandgap photodetection observed in 2D-RPPs not only opens avenues for future explorations of

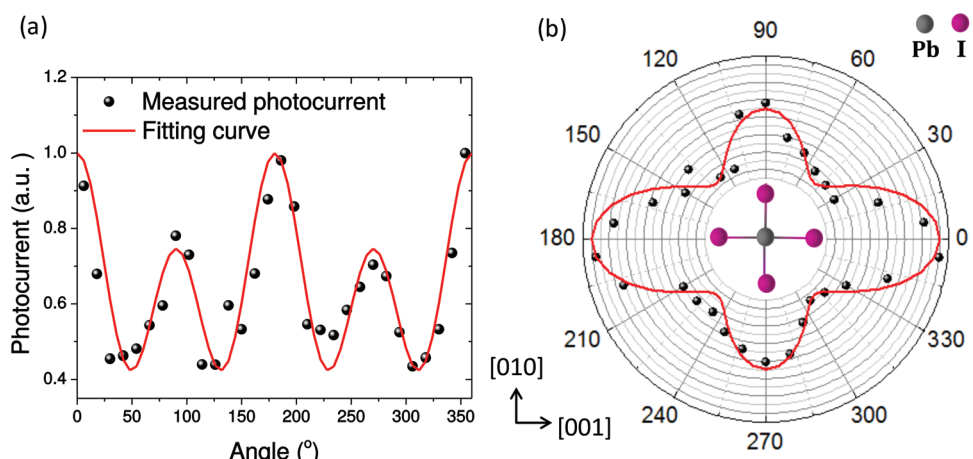


**Figure 4.** a,b) Measured photocurrent under linearly polarized illumination at  $\lambda = 1200$  nm as a function of the half-wave-plate angle for the 2D-RPP (I<sub>n=4</sub>) device. The red lines are fitted curves.

nonlinear optics in this class of hybrid quantum materials but also suggests its potential use in nonlinear photonic and optoelectronic applications.

## Experimental Section

**Device Fabrication:** Field effect transistor (FET) devices on 285 nm SiO<sub>2</sub>/Si substrates were fabricated by standard electron beam lithography (EBL), thermal evaporation, and liftoff. The graphene patterns were first defined using EBL with a polymethylmethacrylate positive resist as an etch mask. Metal electrodes were then deposited through thermal evaporation of Cr (3 nm)/Au (5 nm) and a subsequent liftoff step was employed to wash away the resist. For the 2PPL measurements, the 2D-RPP crystals were mechanically exfoliated onto clean quartz substrates using the Scotch-tape method. For the optoelectronic measurements, the bulk RPP crystals were first exfoliated on polydimethylsiloxane and uniform perovskite flakes were then selected and transferred onto the prepatterned FET electrodes using a transfer stage. The exfoliation and transfer processes were carried out in an argon-filled glove box. The transferred RPP flakes were covered with a thin layer of h-BN before taking out of the glove box for optical and optoelectronic characterizations. Atomic force microscopy (AFM) was used to measure RPP-flake thickness.

**Linear- and Nonlinear-Optical Characterizations:** One-photon-excited photoluminescence (1PPL) measurements were performed using a confocal microscope with 473 nm (for 2D-RPP  $I_{n=1}$ ) and 532 nm (for 2D-RPP  $I_{n=2,3,4}$ ) laser excitation wavelengths. The laser beam was focused on the samples using a 100× objective lens, and the photoluminescence (PL) signals were collected at a backscattering angle with the same objective lens. The PL emission was routed via a bundled optical fiber to a monochromator (Acton, Spectra Pro 2300i) coupled to a charge-coupled device (CCD) (Princeton Instruments, Pixis 400B).

For the two-photon-excited PL (2PPL) measurements, a confocal microscope combined with a laser system (Light Conversion Ltd, pulse duration of 110 fs, excitation wavelength of 1030 nm, and repetition rate of 1 MHz) was used. The laser beam was reflected by a short-pass dichroic mirror (Di02-R635-Semrock-25 × 36) and focused onto the sample ( $\approx 2 \mu\text{m}$  spot size) with an objective lens (Nikon Plan Fluor 20×/0.50, working distance (WD) 2.1 mm). The average power of the laser pulses was measured with an optical power meter (Optical Power Meter 1917-R, Newport). The 2PPL emission was collected in a back-scattering configuration via the same objective and detected by a spectrometer (Model Ocean Optics QEPro). For polarization-dependent 2PPL measurements, the orientation of the linear polarized laser pulses was varied by a half-wave plate. Positioning the laser spot on an RPP flake was achieved using an imaging system consisting of a white light source (Spectra Products, Xenon Light Source, ASB-XE-175) coupled to a CCD (Model TOUPCAM-UCMOS03100KPA). To obtain the D-2PA coefficients of the 2D-RPPs, the 2PPL signal from a CdS crystal was measured under the same conditions and setup as a reference.

**Sub-Bandgap Photodetection Measurements:** A Ti:sapphire femtosecond laser system (Coherent Inc., Libra, 150 fs, 800 nm, 1 kHz) was used as a pump of an optical parametric generator/amplifier (Coherent Inc., TOPAS-C) for the generation of near-infrared laser pulses (800–1600 nm with a step of 50 nm). The 2D-RPP device was loaded into a vacuum chamber (air pressure  $< 10^{-3}$  Torr), in order to mitigate noise from ionized molecules drifting on the top of, or through the h-BN layer. The laser pulses were focused onto the device channel through a window using a lens. The photocurrent was measured by a source-meter (KEITHLEY 2636B), when the 2D-RPP device was positioned at the focal plane of the laser pulses, where a maximal photocurrent was observed. In the polarization-dependent 2 PC measurements, the same half-wave plate was used to vary the orientation of the linearly polarized laser pulses.

## Supporting Information

Supporting Information is available from the Wiley Online Library or from the author.

## Acknowledgements

F.Z., I.A., and L.K. contributed equally to this work. F.Z. carried out the theoretical calculations, conducted optical characterization and data analysis. I.A. fabricated all 2D-RPPs based phototransistors, prepared all the samples for 2PPL, and performed 1PPL and AFM measurements. K.L. synthesized all single crystals of 2D-RPPs. All authors contributed to the overall scientific interpretation. Financial supports from Ministry of Education/National University of Singapore (MOE/NUS) grant R144-000-401-114 are acknowledged. K.P.L. acknowledges support from the National Research Foundation, Prime Minister's Office, Midsized Centre program (CA2DM), Singapore.

## Conflict of Interest

The authors declare no conflict of interest.

## Keywords

2D Ruddlesden-Popper perovskites, excitonic effects, nonlinear optics, sub-bandgap photodetection, two-photon absorption

Received: July 1, 2019

Revised: August 30, 2019

Published online: October 8, 2019

- [1] R. W. Boyd, *Nonlinear Optics*, 3rd ed., Academic Press, Burlington, MA, USA **2008**.
- [2] L. Chrostowski, M. Hochberg, *Silicon Photonics Design: From Devices to Systems*, Cambridge University Press, Cambridge, UK **2015**.
- [3] D. A. Fishman, C. M. Cirloganu, S. Webster, L. A. Padilha, M. Monroe, D. J. Hagan, E. W. Van Stryland, *Nat. Photonics* **2011**, 5, 561.
- [4] R. Prakash, O. Yizhar, B. Grewe, C. Ramakrishnan, N. Wang, I. Goshen, A. M. Packer, D. S. Peterka, R. Yuste, M. J. Schnitzer, K. Deisseroth, *Nat. Methods* **2012**, 9, 1171.
- [5] T. Tanaka, M. Miyabara, Y. Nagao, K. Saito, Q. Guo, M. Nishio, K. M. Yu, W. Walukiewicz, *Appl. Phys. Lett.* **2013**, 102, 052111.
- [6] D. Sun, G. Aivazian, A. M. Jones, J. S. Ross, W. Yao, D. Cobden, X. Xu, **2012**, 7, 114.
- [7] M. A. W. van Loon, N. Stavrias, NguyenH. Le, K. L. Litvinenko, P. T. Greenland, C. R. Pidgeon, K. Saeedi, B. Redlich, G. Aepli, B. N. Murdin, *Nat. Photonics* **2018**, 12, 179.
- [8] G. S. He, *Nonlinear Optics and Photonics*, OUP, Oxford, UK **2014**.
- [9] M. Piccardo, N. A. Rubin, L. Meadowcroft, P. Chevalier, H. Yuan, J. Kimchi, F. Capasso, *Appl. Phys. Lett.* **2018**, 112, 041106.
- [10] D. L. Boiko, A. V. Antonov, D. I. Kuritsyn, A. N. Yablonskiy, S. M. Sergeev, E. E. Orlova, V. V. Vaks, *Appl. Phys. Lett.* **2017**, 111, 171102.
- [11] L. Dou, A. B. Wong, Y. Yu, M. Lai, N. Kornienko, S. W. Eaton, A. Fu, C. G. Bischak, J. Ma, T. Ding, N. S. Ginsberg, L.-W. Wang, A. P. Alivisatos, P. Yang, *Science* **2015**, 349, 1518.
- [12] H. Tsai, W. Nie, J.-C. Blancon, C. C. Stoumpos, R. Asadpour, B. Harutyunyan, A. J. Neukirch, R. Verduzco, J. J. Crochet, S. Tretiak, L. Pedesseau, J. Even, M. A. Alam, G. Gupta, J. Lou, P. M. Ajayan, M. J. Bedzyk, M. G. Kanatzidis, A. D. Mohite, *Nature* **2016**, 536, 312.

- [13] S. Yang, W. Niu, A.-L. Wang, Z. Fan, B. Chen, C. Tan, Q. Lu, H. Zhang, *Angew. Chem., Int. Ed.* **2017**, *56*, 4252.
- [14] J. Song, L. Xu, J. Li, J. Xue, Y. Dong, X. Li, H. Zeng, *Adv. Mater.* **2016**, *28*, 4861.
- [15] J. Even, L. Pedesseau, C. Katan, *J. Phys. Chem. C* **2014**, *118*, 11566.
- [16] O. Yaffe, A. Chernikov, Z. M. Norman, Y. Zhong, A. Velauthapillai, A. van der Zande, J. S. Owen, T. F. Heinz, *Phys. Rev. B* **2015**, *92*, 045414.
- [17] C. C. Stoumpos, D. H. Cao, D. J. Clark, J. Young, J. M. Rondinelli, J. I. Jang, J. T. Hupp, M. G. Kanatzidis, *Chem. Mater.* **2016**, *28*, 2852.
- [18] I. Abdelwahab, P. Dichtl, G. Grinblat, K. Leng, X. Chi, I.-H. Park, M. P. Nielsen, R. F. Oulton, K. P. Loh, S. A. Maier, *Adv. Mater.* **2019**, *31*, 1902685.
- [19] I. Abdelwahab, G. Grinblat, K. Leng, Y. Li, X. Chi, A. Rusydi, S. A. Maier, K. P. Loh, *ACS Nano* **2018**, *12*, 644.
- [20] K. F. Mak, S. Jie, *Nat. Photonics* **2016**, *10*, 216.
- [21] F. Zhou, W. Ji, *Opt. Lett.* **2017**, *42*, 3113.
- [22] F. Zhou, J. H. Kua, S. Lu, W. Ji, *Opt. Express* **2018**, *26*, 16093.
- [23] J.-C. Blancon, A. V. Stier, H. Tsai, W. Nie, C. C. Stoumpos, B. Traoré, L. Pedesseau, M. Kepenekian, F. Katsutani, G. T. Noe, J. Kono, S. Tretiak, S. A. Crooker, C. Katan, M. G. Kanatzidis, J. J. Crochet, J. Even, A. D. Mohite, *Nat. Commun.* **2018**, *9*, 2254.
- [24] K. Tanaka, T. Takahashi, T. Kondo, K. Umeda, K. Ema, T. Umebayashi, K. Asai, K. Uchida, N. Miura, *Jpn. J. Appl. Phys.* **2005**, *44*, 5923.
- [25] F. O. Saouma, C. C. Stoumpos, J. Wong, M. G. Kanatzidis, J. I. Jang, *Nat. Commun.* **2017**, *8*, 742.
- [26] K. Leng, I. Abdelwahab, I. Verzhbitskiy, M. Telychko, L. Chu, W. Fu, X. Chi, N. Guo, Z. Chen, Z. Chen, C. Zhang, Q.-H. Xu, J. Lu, M. Chhowalla, G. Eda, K. P. Loh, *Nat. Mater.* **2018**, *17*, 908.
- [27] J.-C. Blancon, H. Tsai, W. Nie, C. C. Stoumpos, L. Pedesseau, C. Katan, M. Kepenekian, C. M. M. Soe, K. Appavoo, M. Y. Sfeir, S. Tretiak, P. M. Ajayan, M. G. Kanatzidis, J. Even, J. J. Crochet, A. D. Mohite, *Science* **2017**, *355*, 1288.
- [28] F. P. G. de Arquer, A. Armin, P. Meredith, E. H. Sargent, *Nat. Rev. Mater.* **2017**, *2*, 16100.
- [29] J. Huang, Y. Yuan, Y. Shao, Y. Yan, *Nat. Rev. Mater.* **2017**, *2*, 17042.
- [30] D. C. Hutchings, B. S. Wherrett, *Phys. Rev. B* **1994**, *49*, 2418.
- [31] K. Yan, Z. Wei, J. Li, H. Chen, Y. Yi, X. Zheng, X. Long, Z. Wang, J. Wang, J. Xu, S. Yang, *Small* **2015**, *11*, 2269.
- [32] P. You, Z. Liu, Q. Tai, S. Liu, F. Yan, *Adv. Mater.* **2015**, *27*, 3632.
- [33] K. He, N. Kumar, L. Zhao, Z. Wang, K. F. Mak, H. Zhao, J. Shan, *Phys. Rev. Lett.* **2014**, *113*, 026803.
- [34] V. D'Innocenzo, G. Grancini, M. J. P. Alcocer, A. R. S. Kandada, S. D. Stranks, M. M. Lee, G. Lanzani, H. J. Snaith, A. Petrozza, *Nat. Commun.* **2014**, *5*, 3586.
- [35] Z. Liu, Y. Gong, W. Zhou, L. Ma, J. Yu, J. C. Idrobo, J. Jung, A. H. MacDonald, R. Vajtai, J. Lou, P. M. Ajayan, *Nat. Commun.* **2013**, *4*, 2541.
- [36] C. Melios, A. Centeno, A. Zurutuza, V. Panchal, C. E. Giusca, S. Spencer, S. R. P. Silva, O. Kazakova, *Carbon* **2016**, *103*, 273.
- [37] L. E. Shea-Rohwer, E. M. James, *J. Lumin.* **2007**, *127*, 499.
- [38] G. Walters, B. R. Sutherland, S. Hoogland, D. Shi, R. Comin, D. P. Sellan, O. M. Bakr, E. H. Sargent, *ACS Nano* **2015**, *9*, 9340.
- [39] F. O. Saouma, D. Y. Park, S. H. Kim, M. S. Jeong, J. I. Jang, *Chem. Mater.* **2017**, *29*, 6876.
- [40] R. Murgan, D. R. Tilley, Y. Ishibashi, J. F. Webb, J. Osman, *J. Opt. Soc. Am. B* **2002**, *19*, 2007.